Impact of α-synuclein fibrillar strains and β-amyloid assemblies on mouse cortical neurons endo-lysosomal logistics

Qiao-Ling Chou, Ania Alik, François Marquier, Ronald Melki, François Treussart, Michel Simonneau

eNeuro Accepted Manuscript

1 **Manuscript Title**: Impact of α-synuclein fibrillar strains and ß-amyloid
2 assemblies on mouse cortical neurons endo-lysosomal logistics
3
4 **Abbreviated Title**: Protein assemblies and neurons endo-lysosomal logistics
5

6 **List all Authors**: Qiao-Ling Chou[1], Ania Alik[2], François Marquier[1], Ronald Melki[2],
7 François Treussart[1,*] & Michel Simonneau[1,3,*]
8 [1] Université Paris-Saclay, ENS Paris-Saclay, CNRS, CentraleSupélec, LuMIn, 91190
9 Gif-sur-Yvette, France.
10 [2] Laboratory of Neurodegenerative Diseases, Institut François Jacob (MIRCen),
11 CNRS, CEA, Université Paris-Saclay, 92265 Fontenay-aux-Roses cedex, France.
12 [3] Département d'Enseignement et de Recherche en Biologie, ENS Paris-Saclay,
13 91190 Gif-sur-Yvette, France.
14 * co-senior authors

15
16 **Author contribution**: Q-LC, FT, and MS designed research; Q-LC performed research and
17 analyzed data; AA and RM contributed reagents; FM contributed analytic tools; MS, Q-LC and FT
18 wrote the paper.

19 Corresponding authors: Correspondence should be addressed to François Treussart
20 (francois.treussart@ens-paris-saclay.fr) or Michel Simonneau
21 (michel.simonneau926@gmail.com)

22
23 **Number of figures**: 8 main + 8 extended figures
24 **Number of tables**: 0
25 **Number of words**:
26   Abstract: 257
27   Significant statement: 115
28   Introduction: 416
29   Discussion: 1187
30

Abstract

Endosomal transport and positioning cooperate in the establishment of neuronal compartment architecture, dynamics and function, contributing to neuronal intracellular logistics. Furthermore, dysfunction of endo-lysosomal has been identified as a common mechanism in neurodegenerative diseases. Here, we analyzed endo-lysosomal transport when α-synuclein (α-syn) fibrillar polymorphs, ß-amyloid (Aß) fibrils and oligomers were externally applied on primary cultures of mouse cortical neurons. To measure this transport, we used a simple readout based on the spontaneous endocytosis in cultured neurons of fluorescent nanodiamonds, a perfectly stable nano-emitter, and the subsequent automatic extraction and quantification of their directed motions at high-throughput. α-syn fibrillar polymorphs, Aß fibrils and oligomers induce a two-fold decrease of the fraction of nanodiamonds transported along microtubules, while only slightly reducing their interaction with cortical neurons. This important decrease in moving endosomes is expected to have a huge impact on neuronal homeostasis. We next assessed lysosomes dynamics, using Lysotracker. Neurons exposure to Aß oligomers led to an increase in the number of lysosomes, a decrease in the fraction of moving lysosome and an increase in their size, reminiscent of that found in APP transgenic model of Alzheimer's disease. We then analyzed the effect of α-syn fibrillar polymorphs, Aß fibrils and oligomers on endosomal and lysosomal transport and quantified directed transport of those assemblies within cortical neurons. We report different impacts on endosomal and lysosomal transport parameters and differences in the trajectory lengths of cargoes loaded with pathogenic protein assemblies. Our results suggest that intraneuronal pathogenic protein aggregates internalization and transport may represent a target for novel neuroprotective therapeutic strategies.

Significance Statement

Neurodegenerative diseases (NDs) are characterized by the deposition of protein aggregates. These proteins exert a broad range of neuronal toxicity. Defects in endo-lysosomal traffic are increasingly viewed as key pathological features of NDs, likely contributing to synaptic dysfunction and ultimately neuronal death. Here we measured by fast fluorescence videomicroscopy the endosomal and lysosomal dynamics in the branches of primary culture of mouse cortical neurons after externally applying α-syn fibrillar polymorphs (fibrils and ribbons) and Aß assemblies (oligomers and fibrils). We provide significant insight into the differential effects of these pathogenic protein assemblies on endosomal and lysosomal transport, and also reveal distinct transport characteristics of the compartments loaded with these protein assemblies compared to endosome ones.

Introduction

Impairment of axonal transport has recently emerged as a factor shared by several neurodegenerative disorders (Millecamps and Julien, 2013; Morfini et al., 2009). Early impact on intraneuronal transport has been thus proposed as a phenotypic trait common to neurodegenerative diseases such as Alzheimer's, Huntington's and Parkinson's Disease (Stokin et al., 2005; Saudou and Humbert, 2016; Volpicelli-Daley et al., 2014). There is compelling evidence that abnormal protein accumulation in the brain is a key pathophysiological mechanism underlying the neurotoxicity observed in these age-related disorders (Golde et al., 203; Soto et al., 2018). Selective aggregation of misfolded proteins is a hallmark of these neurodegenerative diseases (Saez-Atienzar & Masliah, 2020). An important level of complexity is due to

3

93 the fact that different species of the same molecules, such as oligomers and fibrils,

94 contribute to a whole spectrum of toxicities (Alam et al., 2017).

95 Few studies have compared, within the same neurons, fibrillary and oligomeric α-

96 synuclein (α-syn) and ß-amyloid (Aß) which are known to be involved in Parkinson

97 and Alzheimer's diseases respectively. Brahic et al., 2016, demonstrated for instance

98 that α-syn, $Aß_{42}$ and HTTExon1 fibrils are transported anterogradely and retrogradely

99 in mice primary neurons grown in microfluidic chambers with different efficiencies in

100 axons. Here, we thoroughly quantified the impact of two α-syn fibrillar polymorphs

101 namely fibrils (α-synF) and ribbons (α-synR), $Aß_{42}$ fibrils (AßF) and oligomers (AßO)

102 on endosomal and lysosomal transports in primary cultures of mouse neurons. To

103 measure this transport and investigate finely its parameters, we relied on our

104 previously established method (Haziza et al., 2017), in which we let perfectly stable

105 and non-toxic fluorescent nanodiamonds (FND) being spontaneously internalized by

106 neurons in endosomes, then follow their displacement by fast video-microscopy and

107 finally apply to the videos our analysis pipeline to extract and analyze single particle

108 trajectories automatically. Using fluorescently-labelled α-syn and Aß assemblies, we

109 conducted the same investigations on their own intraneuronal transport.

110 Our data allow to address three complementary questions: (i) do α-synF, α-synR,

111 AßF and AßO influence the fraction of cargoes moving along the microtubules; (ii) do

112 they impact the dynamics of intracellular endosomal and lysosomal transport.

113 We show here that all pathogenic proteins assemblies reduce the fraction of

114 endosomes moving along microtubules and impact some of their transport

115 parameters. Furthermore, lysosomes properties (number, fraction of lysosomes

116 moving and transport parameters) are also affected by AßO. Finally, our data indicate

117 that cargoes loaded with α-synF, α-synR, AßF or AßO are transported differently

4

118 from endosomes, considered as control cargoes, which suggests distinct molecular

119 characteristics of cargo-motor assemblies.

Material and Methods

121 **Production of α-syn fibrillar assemblies, Aß fibrils and oligomers**

122 The expression and purification of human WT α-syn was performed as previously

123 described (Ghee et al., 2005). Pure WT α-syn was incubated in buffer A to obtain the

124 fibrillar polymorph ''fibrils'' α-synF (50 mM Tris-HCl at pH 7.5, 150 mM KCl) and in

125 buffer B for ''ribbons'' α-synR (5 mM Tris-HCl at pH 7.5) at 37°C under continuous

126 shaking in an Eppendorf Thermomixer (Hamburg, Germany) set at 600 rotations per

127 minute (rpm) for 4–7 days (Bousset et al., 2013). The fibrillar α-syn polymorphs were

128 centrifuged twice at 15,000 g for 10 min and resuspended twice in phosphate-

129 buffered saline (PBS) at 1,446 g/L prior to labeling with ATTO 488 NHS-ester (#AD

130 488-3, Atto-Tec, Siegen, Germany) fluorophore following the manufacturer's

131 instructions using a protein/dye ratio of 1:2. The labeling reactions were arrested by

132 addition of 1 mM Tris (pH 7.5). The unreacted fluorophore was removed by a final

133 cycle of two centrifugations at 15,000 g for 10 min and resuspensions of the pellets in

134 PBS. This labeling protocol typically yields ≥ 1 ATTO molecule incorporated per α-

135 syn monomer on average as previously demonstrated (Shrivastava et al., 2015). The

136 assemblies were examined by transmission electron microscopy after adsorption on

137 200 mesh carbon-coated electron microscopy grids and negative stained with 1%

138 uranyl acetate before and after fragmentation using a JEOL 1400 electron

139 microscope (JEOL, Tokyo, Japan).

140 The expression and purification of Met-Aß 1-42 was performed as described (Walsh

141 et al., 2009). Aß was assembled in PBS, at 4°C or 37°C without shaking for 2 or 24 h

142 to obtain oligomers AßO or fibrils AßF, respectively. The two kinds of assemblies

5

143 were labeled with ATTO 488 NHS-ester at a protein/dye ratio of 1:2. The labeling

144 reactions were arrested by addition of 1 mM Tris at pH 7.5. For fibrillar Aß, the

145 unreacted fluorophore was removed by two cycles of centrifugation and resuspension

146 of the pelleted fibrils in PBS as described for α-syn. For oligomeric Aß, the oligomers

147 were separated from the monomeric and fibrillar forms of the protein by size

148 exclusion chromatography on a Superose 6 HR10/300 column (GE Healthcare, Life

149 Sciences, Wauwatosa, WI, USA) equilibrated in PBS pH 7.4 at a flow rate of

150 0.5 mL/min. Elution was monitored by measuring absorbance at 280 nm wavelength.

151 The Superose 6 column was calibrated with Dextran blue (over 2200 kDa), (670 kDa),

152 β -amylase (200 kDa), BSA (66 kDa), and carbonic anhydrase (29 kDa) standards

153 (Sigma-Aldrich).

154 **Primary mouse cortical neuron cultures**

155 We used commercial primary mouse cortical neurons (ref. Gibco A15586,

156 ThermoFisher) because the provider quality check guarantees a purity of 98% of

157 neurons. The cells were grown on high optical quality glass coverslips (high-precision

158 170±5 µm thick, 18 mm diameter, ref. 0117580, Marienfeld GmbH, Germany). The

159 coverslips are first cleaned with 70% ethanol, rinsed with water for injection (ref.

160 A128730, ThermoFisher Inc., USA) and exposed during 1 h to UV light. They were

161 then coated with 0.1 mg/ml poly-L-ornithine (ref. P3655, Sigma-Aldrich Merck KGaA,

162 Germany) and placed for 2 h in an incubator set at 37°C, then rinsed twice with water

163 and let dry at biological hood for one hour. We plated an amount of 6×10^5 primary

164 mouse cortical neurons (ref. Gibco A15586, ThermoFisher) on each coated coverslip,

165 which was then put at the bottom of a 6-wells plate, each well-being finally filled with

166 3 mL of neurobasal phenol red-free medium (ref. 12348017, ThermoFisher)

167 containing 0.5 mM GlutaMax (ref. 35050061 ThermoFisher), 2% B-27 (ref. 17504044,

6

168 ThermoFisher) and 1% PenStrep (ref. 15070063, ThermoFisher). The 6-well plate

169 was then placed in an incubator at 37 °C and 5% CO_2. Half of the volume of the

170 medium was replaced with fresh medium 24 h after plating. We made the subsequent

171 medium changes every 3 days to reduce glutamate toxicity. Neurons were grown

172 until 21 days in culture.

173 **Exposure of mouse cortical neurons to α-syn fibrillar assemblies, Aß fibrils or**

174 **oligomers**

175 In all the measurements dealing with (1) the impact of pathogenic protein assemblies

176 on endosomal-lysosomal transport, (2) their colocalization with FND-labelled

177 compartment or lysosomes, or (3) the tracking of their intraneuronal transport by

178 fluorescence videomicroscopy, cortical neurons were incubated with either 0.2 μM

179 ATTO 488-labeled α-synF or R, or 1 μM ATTO 488-labeled AßF or AßO.

180 α-synF or R were added at 24 h, 48 h, or 72 h before observations, while the addition

181 time was either 24 h or 48 h for ATTO 488-labeled AßF or AßO. The video

182 acquisitions of all the experiments were performed at DIC21.

183 **Washing protocol to test the protein assemblies interaction with the neuron**

184 **membrane**

185 The coverslip with the culture attached to them, were extracted from the well and

186 flushed with PBS first and then twice with culture medium, before FND internalization

187 was carried out following the procedure described in the next paragraph.

188 **Intraneuronal transport cargo labeling**

189 To evaluate the endosomal transport parameters, we relied on our fluorescent

190 nanodiamond assay (Haziza *et al.* 2017). We used commercially available sized

191 35 nm FND (brFND-35, FND Biotech, Taiwan). Each NP contains an average of 15

7

192 nitrogen-vacancy emitters displaying a peak emission wavelength around 700 nm

193 and a full-width at half-maximum of ≈100 nm. This far-red emission allows also to

194 investigate   the   colocalization   of   green-emitting   ATTO   488-labelled

195 neurodegenerative-disease related species with FND-labeled cargos. FND were

196 internalized in cortical neurons just before the transport analysis, at DIC21. Each

197 culture coverslip was removed from the 6-well plate containing maintaining medium

198 and put in contact with 400 µL of fresh culture medium to which we added 2 μl of

199 stock solution of FNDs (1 mg/mL), reaching a final FND concentration of 5 μg/mL.

200 After 10 mins incubation, the extra FND-containing medium was absorbed by a wiper

201 sheet and the coverslip was placed back to the dish containing the old maintaining

202 medium. The culture was then placed back during 20 mins in the incubator before the

203 video acquisition.

204 To   measure   lysosomal   transport   or   investigate   the   colocalization   of

205 neurodegenerative disease-related species with lysosomes, cortical neurons were

206 stained at DIC21, just before the observation, with LysoTracker Deep Red (ref.

207 L12492, ThermoFisher) or Magic Red Cathepsin B substrate (ref. ICT937, Bio-Rad).

208 These dye molecules have an emission spectrum within the similar range than the

209 one of FND. The coverslip was removed from maintaining medium and incubated

210 with prewarmed (37°C) culture medium containing 50 nM LysoTracker or Magic Red

211 (1:20 dilution) for 1 h. The probe-containing medium was replaced with the old

212 maintaining medium and followed by video acquisition.

213 **Pseudo-total internal reflection (TIRF) live-cell videomicroscopy**

214 Pseudo-TIRF illumination was implemented on an inverted microscope (Eclipse Ti-E,

215 Nikon, Japan) as described in details in (Haziza et al. 2017). The whole microscope

216 is enclosed in a cage incubator (Okolab, Italy) to maintain temperature at 37°C. For

8

217   the intraneuronal transport recording, each coverslip supporting the neuron culture is

218   mounted at the bottom a Ludin chamber (type 1, Life Imaging Service, Switzerland),

219   installed inside the environmental chamber (in which 5% partial CO_2 pressure and

220   100% hydrometry is maintained) having a hole at its bottom allowing direct optical

221   access of the microscope objective to the coverslip. We used a ×100 magnification

222   and 1.49 numerical aperture immersion oil objective (CFI Apo TIRF ×100 Oil, Nikon),

223   compatible with differential inference contrast (DIC) mode. Field of views of interest

224   of the neuron cultures were selected in white-light illumination DIC mode. Two

225   continuous-wave lasers are coupled to the microscope and fluorescence was

226   recorded on a cooled EMCCD array detector (DU-885K-CS0, Andor Technologies,

227   UK) of 1004×1002 pixels, with 80 nm pixel size in the sample plane. Two-minutes

228   duration videos were acquired at 20 full frame/s rate large enough to be able to

229   detect short pausing duration in cargoes displacements. EMCCD parameters were

230   selected to provide the largest signal-to-background ratio for FND label tracking at

231   the selected frame rate, leading to EM gain of 90, preamplification gain ×3.8, and

232   digitalization speed of 35 MHz. FNDs and Lysotracker fluorophore were excited with

233   a diode-pumped solid-state laser at a wavelength of 561 nm (SLIM-561-100, Oxxius

234   S.A., France), while ATTO 488 dye was excited with a laser diode emitting at a

235   wavelength of 488 nm (LBX-488-200-CSB-PP, Oxxius S.A). Each excitation laser

236   power was adjusted so that the detection dynamic range of all channels was identical

237   for the above mentioned fixed EMCCD settings. This leads to 561 nm laser excitation

238   power of 60 mW for FND, 200 µW for LysoTracker and 1 mW for Magic Red, and to

239   488 nm laser excitation power of 200 µW for ATTO 488 dye.

240   To perform two-color acquisitions and record simultaneously FND (or LysoTracker)

241   and ATTO 488 we combined the two laser beams with a dual-band dichroic filter (ref.

242 Di01-R488/561, Semrock, USA), and placed a dual imaging system (W-VIEW

243 GEMINI, Hamamatsu, Japan) in front of the EMCCD array detector (DU-885K-CS0,

244 Andor Technologies, UK). This system splits half of the detection field of view (FoV)

245 in two color channels with a dichroic beamsplitter (FF560-FDi01, Semrock) and

246 projects each color on half of the array detector, further preceded by bandpass

247 detection filters (red channel: HC697/75, Semrock; green channel: ET525/50,

248 Chroma Corporation, USA). The result is that each frame of the video contains the

249 same rectangular FoV (1004×501 pixels) in green (ATTO 488) and red (FND and

250 LysoTracker) emission range, allowing to identify spots that colocalize dynamically.

251 **Video processing and intraneuronal transport quantification**

252 Two programs written in python were developed to extract quantitative parameters

253 from videos automatically. The first one relies on Trackpy 0.4.2 package (Trackpy

254 2019), from which it uses two functions: `locate` to identify isolated spots in each

255 fluorescence frame and fit them with gaussians, and `link` which connects the spots

256 between frames to form trajectories using Crocker-Grier algorithm (Crocker & Grier

257 1996). Transport parameters are then calculated with a second program which first

258 parses each trajectory into "go" and "stop" phases based on the confinement ratio

259 calculation as described in (Haziza et al., 2017). Four main transport parameters are

260 extracted for each trajectory: velocity, which is the average speed of all go phases;

261 run length: average distance traveled during all go phases; pausing time: average

262 duration of the stop phases, and pausing frequency (events/min). In addition to these

263 four main parameters, we also calculated the total length of the trajectory as the sum

264 of all run lengths during go phases.

265 **Lysosomes size estimation**

266   To get an estimate of the lysosome size from the diffraction limited fluorescence

267   images, we considered the LysoTracker spots as the result of the convolution of the

268   microscope point spread function (assimilated to a gaussian of standard deviation,

269   SD, σ_{PSF}) and the lysosome assimilated to a symmetrical gaussian of SD σ_{L}. The

270   result of this convolution is also a gaussian of SD σ_{T}, related to σ_{L} and σ_{PSF} by

271    $\sigma_{\mathrm{T}}{}^2 = \sigma_{\mathrm{PSF}}{}^2 + \sigma_{\mathrm{L}}^2$. σ_{T} is the so-called "`size`" output of the Trackpy `locate` function.

272   The knowledge of σ_{T} and σ_{PSF} allows the derivation of σ_{L}. We then defined the

273   lysosome "diameter" d_{L} as the full width at half maximum of its gaussian

274   approximation, inferred by $d_{\mathrm{L}} = 2\sqrt{2\ln 2}\,\sigma_{\mathrm{L}}$. For the PSF size σ_{PSF} we took the

275   measured value of the smallest FND spot observed in several trajectories with our

276   microscope. This value was σ_{PSF}=112 nm, consistent with the theoretical Airy radius

277   ρ_{A}=286 nm (diffraction limit at 700 nm maximum emission wavelength for the 1.49

278   numerical aperture objective used), and the empirical relation $\sigma_{\mathrm{PSF}} = \frac{\rho_{\mathrm{A}}}{3}$, giving here

279   an experimental PSF SD of 286/3=95 nm.

280   **Quantification of fluorescence intensity of ATTO 488-labeled α-synF in cortical**

281   **neuron branches**

282   We quantify the fluorescence intensity from the first frame of the green channel

283   videos, using Fiji Image J software (Schindelin et al, 2012). We first identify from the

284   DIC image some well-separated and mainly straight neuronal branches, that we

285   surround with the region-of-interest (ROI) polygonal selection tool as close as

286   possible to the branch to include all the fluorescence signal, over a length of 30 µm.

287   We then used the `Analyze` function to measure the average intensity counts per

288   pixel in the defined ROI, to which we subtract the average background counts,

289   measured after having moved the ROI in a region without branches.

290   **Data representation and statistical analysis**

291 All bar plots display the ± standard error on the mean of the distribution. Box plots

292 display the median value as the horizontal line within the box whose limits are 25%

293 and 75% percentiles; bottom and top horizontal lines correspond to 10% and 90%

294 percentiles. As all the data compared between two conditions were random and

295 normally distributed but with unequal variance (as tested with a *F*-test), we performed

296 the relevant comparison test which is the non-parametric Wilcoxon Mann-Whitney

297 two-tailed (implemented in Igor Pro 8, Wavemetrics Inc., USA). Stars referred to the

298 following *p*-value significance level: *$p<0.05$; **$p<0.01$; ***$p<0.001$.

Results

Quantification of intraneuronal transport using fluorescent nanodiamonds

301 We quantified the intraneuronal transport with our FND tracking assay (Haziza et al.,

302 2017). We first used a simple readout consisting in counting the number of FND

303 detected in field-of-views (FoV) of size 40×80 μm during 2 minutes. We selected

304 each FoV based on the criteria that it contains approximately the same density of

305 neuronal branches, as estimated from differential interference contrast images

306 (Fig. 1). Our incubation protocol was designed to strongly limit any non-specific

307 interactions of FND, like their attachment to the coverslip supporting the culture, and

308 favor their interaction with neuron membranes and their subsequent internalization in

309 endosomes (Haziza et al., 2017). The perfectly stable fluorescence of FND allows to

310 reconstruct the endosome trajectories accurately and identify "go" and "stop" (none or

311 very slow motion) phases (Fig. 1B) in the transport of FND-labelled endosomes along

312 neuronal branches as observed in differential interference contrast microscopy

313 (Fig. 1C).

α-synF and R affect the number of cargos transported along microtubules without major changes in trajectory length

Primary cultures of mouse cortical neurons were incubated at day in culture (DIC) 20 with α-synF or R at a concentration of 0.2 µM for 24 hours. The intraneuronal transport in these cultures was investigated at DIC21.

Both exposures to α-synF or R led to a small decrease (26% for α-synF and 13% for α-synR) in the number of FND (moving or not) present in each FoV, indicating that both fibrillar polymorphs impact the FND binding to neuronal membrane and their transport dynamics within neurons (Fig. 2*A*). Indeed, if we consider the fraction of these FND having a directed motion, corresponding to those being first internalized in endosomes and then taken in charge by molecular motors, we observed that it decreases by 49%, upon exposure of neurons to α-synF and 45% in the case of α-synR (Fig. 2*B*). The unknown mechanism involved in such a large decrease in the number of cargoes transported along microtubules is expected to impair the functions of cortical neurons.

In order to determine if this important reduction of FND moving fraction is related to the binding of the protein assemblies to the neuronal branches membrane, possibly leading to a reduced endocytosis, we tried in the case of α-synF to wash away the aggregates just before the addition of FND (Materials and Methods), but we found that the interaction of the nanodiamonds with neuron did not change in washed-neuron condition compared to unwashed (Fig. 2-1*A*-*C*); in particular, we did not observe differences in the fraction of moving FND. We concomitantly measured the amount of ATTO 488-labelled assemblies along the neuronal branches (as quantified by the dye fluorescence intensity) and could not see any differences before and after

13

338   washing (Fig. 2-1*D-E*), which is in agreement with FND-neuron interaction results,

339   and indicate a strong binding of α-synF to the neuronal membrane.

340   Using our established FND-based intraneuronal transport assay (Haziza et al., 2017)

341   we detected and quantitatively analyzed the alternation of movement and pause

342   phases of intraneuronal cargoes motion. We first measured the length of trajectories

343   (see Material & Methods) for control FND, FND in the presence of either α-synF or α-

344   synR and we did not evidence any major changes (Fig. 2*C*, Fig. 2*D*; decrease of 4%

345   for α-synF and 5% for α-synR).

346   We then measured four parameters: the curvilinear velocity of each moving phase, its

347   run length, the duration of the pauses and the pausing frequency. The velocity

348   (Fig. 2*E*) and run length (Fig. 2*F*) increases (velocity: 31% and 38%; run length: 80%

349   and 100%, for α-synF and R respectively), the pausing time decreases (Fig. 2*G*; 40%

350   decrease for both fibrillar assemblies) while the pausing frequency increases (Fig. 2*H*;

351   19% and 25%, for α-synF and R respectively). These results are summarized in

352   Fig. 2-2A.

353   We next analyzed the same parameters for lysosomes labelled with Lysotracker red,

354   an established marker of lysosomes, with the difference, compared to FND, that all

355   the fluorescent spots, including the static ones, correspond to lysosomes because

356   Lysotracker only become fluorescent once inside lysosomes. α-synR treatment

357   induces a slight but significant decrease (15%) in the number of lysosomes per field-

358   of-view, while α-synF does not (Fig. 3*A*). This result suggests that α-synR reduce the

359   endocytosis. It is consistent with the observed decrease of FND interacting with

360   neuron (Fig. 2*A*) that possibly reveals their reduced uptake. Furthermore, like for

361   endosomes (Fig. 2*B*), α-synF and R induce a 46% and 32% decrease respectively

362   (resp.) in the fraction of lysosomes having a directed motion (Fig. 3*B*). Analysis of

363   lysosome trajectory lengths indicates a slight decrease (Fig. 3*C*; 9% and 3% for α-

364   synF and R resp.). Example of FoV showing lysosome trajectories in the different

365   conditions are shown in Fig. 3*D*, where the large decrease in the fraction of

366   lysosomes having a directed motion can be clearly seen.

367   We quantified the same transport parameters for lysosomes than for FND, using the

368   same experimental paradigm. In contrast to what we observed for endosomes

369   transport, exposure of neurons to α-synF did not lead to any changes in lysosomes

370   transport parameters (Fig. 3*E-H*). Interestingly however, in cortical neurons exposed

371   to α-synR, we measured a slight increase of 6% in lysosomes velocity (Fig. 3*E*) and

372   larger one of 26% in run length (Fig. 3*F*), no significant change in pausing time (Fig.

373   3*G*) and a slight increase of 4% in pausing frequency (Fig. 3*H*). These results are

374   summarized in Fig. 2-2B.

375   **Aß assemblies affect the number of cargos transported along microtubules**

376   **without major changes in trajectory length**

377   We also analyzed the same parameters after DIC20 mouse cortical neurons

378   exposure to either AßF or AßO, for 24 hours, followed by intracellular transport

379   measurement at DIC21. We used the common 1 µM concentration that has been

380   reported to have a biological impact (Marshall et al., 2020). Figure 4*A* shows a slight

381   decrease (3% and 7% for AßF and AßO resp.) of FND interacting with neurons

382   exposed to AßF or AßO, accompanied by a much larger decrease (56% and 29% for

383   AßF and AßO resp.) of the fraction having directed motions (Fig. 4*B*). FND trajectory

384   lengths stay almost the same for AßF (3% decrease) but are reduced by AßO

385   (Fig. 4*C*, Fig. 4*D*; 13% decrease). We also investigated the effect of Aß assemblies

386   at the smaller concentration of 0.2 µM, identical to the one of α-syn assemblies. Even

387   at this lower concentration, we could detect for both AßF and AßO small decreases

388 (19% and 18% for AßF and AßO resp.) in the number of FND per FoV (Fig. 4-1*A*)

389 and in the fraction of FND having a directed motion (Fig. 4-1*B*; 11% and 18% for AßF

390 and AßO respectively). To summarize, as for α-syn assemblies (Fig. 3), the exposure

391 of cortical neurons to Aß assemblies induce important and significant decreases of

392 the endosomal transport.

393 We then measured more precisely the impact of AßF and AßO on endosomal

394 transports parameters. We observed an increase of FND velocity (Fig. 4*E*; 20% and

395 15% for AßF and AßO resp.) and run length (Fig. 4*F*; 5% and 7% for AßF and AßO

396 resp.), a decrease in their pausing time (Fig. 4*G*; 36% and 12% for AßF and AßO

397 resp.) and an increase of the pausing frequency (Fig. 4*H*; 28% and 15% for AßF and

398 AßO resp.), with effects more pronounced for AßF than for AßO. Interestingly, the

399 same trends of changes were also observed at the lower AßF and AßO concentration

400 of 0.2 μM (Fig. 4-1*C-F*). Let us finally point out that for AßF, the important changes of

401 some transport parameters overall combine in an only very slight decrease in

402 trajectory length as shown in Fig 4*C*, which makes the detailed quantitative analysis

403 performed all the more useful. These results are summarized in Fig. 2-2A.

404 Regarding the impact of Aß on lysosomal transport, we noticed large differences

405 between the two types of assemblies AßF and AßO. In neurons exposed to AßO, the

406 total number of lysosomes detected in a FoV as compared to controls increased by

407 50% (Fig. 5*A*) while it stayed unchanged in case of exposure to AßF. The intracellular

408 transport measurements we performed showed that the fraction of moving lysosomes

409 decreased by 1.6-fold and 5.7-fold in neurons exposed to AßF and AßO, respectively

410 (Fig. 5B; from 23% for control to 14% for AßF and 4.5% for AßO). Lysosome

411 trajectory lengths were only slightly decreased for AßF (5%) and more significantly

412 reduced for AßO (Fig. 5C and Fig. 5D; 17% decrease) exposure.

413   We also measured lysosome transport parameters in the presence of 1 μM AßF or

414   AßO (Fig. 5E-H). For AßF, we observed almost no change in velocity (Fig. 5E),

415   pausing time (Fig. 5G), and pausing frequency (Fig. 5H). In contrast, exposure to

416   AßO, led to a 1.7-fold increase of the pausing time. The run length decreased

417   significantly for both assemblies (Fig. 5F; with 9% and 13% decrease for AßF and

418   AßO exposure resp.). These results are summarized in Fig. 2-2B.

419   Furthermore, as changes in lysosome size was described in APP mouse transgenic

420   model of Alzheimer's disease (Gowrishankar et al., 2015), we asked if detectable

421   changes in lysosome diameter can be quantified upon 24 or 48 h exposure to 1 μM

422   AßF and AßO. We detected a slight increase (7%) of lysosome diameter upon

423   exposure of neurons to AßF at 24 h that disappears at 48 h. This contrasts with the

424   increase we observed at both time points (11% and 7% at 24 h and 48 h resp.) in

425   neurons exposed to 1 μM AßO (Fig. 5*I-J* and Fig. 5-1*A-C*). The finding that AßO

426   addition triggers an increase in lysosomes number and size and a decrease in

427   lysosome movements is in agreement with previous reports (Gowrishankar et al.,

428   2015; Marshall et al., 2020).

429   Finally, as LysoTracker can also label other acidic compartments than lysosomes, in

430   particular late endosomes, we repeated the transport experiment with Magic Red

431   substrate that reveals by fluorescence the Cathepsin B protease activity, taking place

432   more specifically in lysosomes. We observed that for both α-synF (Fig. 5-2) and AßF

433   (Fig. 5-3) Magic Red-labelled compartments (lysosomes) behaved the same as

434   LysoTracker-labelled ones for all parameters, with in particular a ≈40% decrease of

435   the mobile fraction of Magic Red and LysoTracker-labelled compartment in the

436   presence of the fibrillar assemblies, and similar colocalization data at 24 h, *i.e.* small

437   colocalization of 4-7% for α-synF compared to 40% for AßF. These results indicates

17

438   that, in our case, LysoTracker and Magic Red labeling largely overlap and that we

439   can rely on LysoTracker puncta density to quantify endocytic activity as we did.

440   These results are summarized in Fig. 2-2C.

441   **Transport of α-syn and Aß assemblies within cortical neurons.**

442   We also assessed α-syn and Aß assemblies transport within cortical neurons while

443   documenting their impact on endosomes and lysosomes dynamics. As ATTO 488

444   dye used to label α-syn and Aß assemblies exhibit no emission spectrum overlap

445   with neither FND nor Lysotracker deep red, we were able to measure simultaneously

446   the transport properties of endosome or lysosome and the assemblies on two-color

447   channels.

448   We first studied α-syn fibrillar assemblies transport (Fig. 6). We found that α-synF

449   and R display directed movements as shown by examples of trajectories in Fig. 6*A-B*.

450   We compared these motions to the endosomal transport in the presence of α-syn

451   fibrillar polymorphs. Interestingly, α-syn F and R trajectories are about 29% shorter

452   than those of FND (Fig. 6*C*). We also compared the transport parameters and found

453   smaller velocity (Fig. 6*D*; 5% and 10% for α-synF and α-synR resp.), run length

454   (Fig. 6*E*; 39% and 46% for α-synF and α-synR resp.) and pausing time (Fig. 6*F*; 19%

455   and 21% for α-synF and α-synR resp.) for α-synF and α-synR-loaded cargoes

456   compared to those of FND-containing endosomes. On the contrary, α-synF and R

457   pausing frequencies were larger than those of FND (Fig. 6*G*; 19% and 8% for α-synF

458   and α-synR resp.). The shorter trajectories length and run-length together with the

459   larger pausing frequency, suggest that cargoes loaded with α-synF- and R are

460   transported less efficiently than those containing FND.

461   Similarly, we also investigated ATTO 488-labelled AßF and AßO intraneuronal

462   transport (Fig. 7) at the concentration of 1 µM, as we could not detect their

18

463   fluorescence signal at 0.2 µM. Both species exhibit directed transport as shown by

464   examples of trajectories in Fig. 7*A-B*. These trajectories are shorter than the ones of

465   FND in the same conditions (Fig. 7*C*), as for α-syn fibrillar assemblies. Regarding the

466   transport parameters, compared to FND, AßF and AßO have slightly larger velocity

467   (Fig. 7*D*; 8% and 12% for AßF and AßO resp.), and a trend towards a shorter run-

468   length (Fig. 7*E*; 7% and 28% for AßF and AßO resp.). As α-syn fibrillar assemblies,

469   AßF and AßO exhibit a much shorter pausing time (Fig. 7*F*; 49% and 53% for AßF

470   and AßO resp.) and a much larger pausing frequency (Fig. 7*G*; 41 and 36% for AßF

471   and AßO resp.). As for α-syn fibrillar assemblies the shorter trajectories length and

472   run-length together with the larger pausing frequency suggest that cargoes loaded

473   with AßF and AßO are transported less efficiently than those containing FND.

474   Moreover, since differences in AßO and AßF uptake in cultured neurons were

475   recently reported (Vadukul et al., 2020), we also investigated the related aspect of

476   the number of Aß assembly trajectories per field-of-view at 24 h and 48 h time points

477   (Fig. 7-1). We did not observe differences in the number of trajectories 24 h after

478   addition of the assemblies (Fig. 7-1*A*) in agreement with Fig. 4B of (Vadukul *et al.*

479   2020). However, at 48 h time point, we measured a ≈2.5 lower number of AßO

480   trajectories compared to AßF ones (Fig. 7-1*B*), which differs to uptake results of

481   (Vadukul *et al.* 2020) at 72 h time point, who reported a ≈1.5 times larger amount of

482   internalized AßO compared to AßF(sonicated). Our observations differ from (Vadukul

483   *et al.* 2020), but several reasons may explain this discrepancy: (i) we quantify only

484   the moving fraction of Aß assemblies; (ii) we do not have the 72 h point, and finally (iii)

485   we do not use the exact same AßF.

486   Finally, we assessed in a quantitative manner the co-localization of α-syn and Aß

487   assemblies with lysosomes, as a function of neuron exposure time at 24 and

488   48 hours (Fig. 8). While the fraction of α-syn fibrillar assemblies moving within

489   lysosomes increases from ≈4% at 24 h to 12-14% at 72 h (Fig. 8*A*), it reaches

490   already ≈41% at 24 h for Aß fibrils continuing its increase up to ≈51% at 48 h

491   (Fig. 8*B*). AßO moving in or with lysosomes have slightly lower colocalization

492   proportions, however much larger than for α-syn fibrillar assemblies. We repeated

493   these analyses with Magic Red labeling instead of LysoTracker for α-synF (Fig. 8-1*A*)

494   and AßF (Fig. 8-1*B*) at 24 h and achieved similar results, with a ≈40% colocalization

495   fraction of AßF with Magic Red-labelled lysosomes, and only ≈7% for α-synF.

Discussion

497   In this work, we investigated the generic effects of α-syn fibrillar polymorphs (fibrils

498   and ribbons) and Aß assemblies (oligomers and fibrils) on endosomal and lysosomal

499   movements in mouse cortical neurons. In neurons, early endosomes and lysosomes

500   move using different types of machinery. Also, the former are compartmentalized

501   (dendrites vs. axon) while the latter are not (Winckler et al., 2018). However, due to

502   the high density of the cultures it was not possible to identify unambiguously the

503   compartment (dendrite or axon) in which the traced vesicles moved, and therefore we

504   could not study separately the impact of the protein assemblies on axonal and

505   dendritic endolysosomal transports.

506   **Potential consequences of a decrease in the number of cargos transported at a**

507   **given time within cortical neuron**

508   The exposure of cortical neurons to α-syn and Aß assemblies led to important

509   reductions (between 32% and 56%) of moving endosomes and lysosomes along

510   neuronal branches (Figs. 1-2). We previously showed that pathogenic α-syn and Aß

511   assemblies bind the plasma membrane with, as a consequence, a redistribution of

512   essential membrane proteins (Renner et al. 2010; Shrivastava et al., 2013;

513   Shrivastava et al., 2015). We further reviewed the physico-pathogenic mechanisms

514   at the origin and resulting from pathogenic proteins assemblies-plasma membrane

515   components interactions (Shrivastava et al., 2017). The reduction we report here

516   might be due to changes in membrane dynamics and endocytosis rate.

517   Exposure of cortical neurons to α-syn and Aß assemblies affected moving FND-

518   containing endosome properties. α-syn fibrillar assemblies increased their velocity by

519   31-38% and run length by 80-100% (Fig. 2*E*-*F*) and decreased their pausing time by

520   40% (Fig. 2*G*) while increasing their pausing frequency to a lesser extend (19-25%,

521   Fig. 2*H*). We observed similar effects but less pronounced for moving FND-

522   containing endosomes when neurons are exposed to AßF or AßO (Fig. 4*E*-*H*). These

523   changes reflect an increase in mobility of moving FND-containing endosomes. Hence,

524   while decreasing the fraction of moving FND-labeled endosomes, α-synF and R or

525   AßF and AßO, increase the overall mobility of the moving ones (Fig. 2-2*A*).

526   A decrease in the number of moving endosomes or lysosomes can affect protein

527   quality control, accompanied by limited elimination of damaged membrane and

528   cytosolic proteins, protein aggregates, and membranous organelles (Winckler et al.,

529   2018). Furthermore, considering that lysosomes and late endosomes act as mRNA

530   translation platforms (Cioni et al., 2019; Liao et al., 2019; Fernandopulle et al., 2021),

531   changes in the number of cargos transported at a given time within a cortical neuron

532   is expected to dramatically impact mRNA translation platform either in dendrites or in

533   axons. In particular, the regulation of protein synthesis and degradation at the

534   neuronal synapse is local and dynamic and modify the synaptic proteome

535   autonomously during plasticity (Giandomenico et al., 2021). Hence, the synaptic

536   function can be impacted if the number of moving lysosomes is affected.

21

Effect of α-syn and Aß assemblies on lysosomes transport

537

538   We observed that α-synF (Fig. 3E-H) and AßF (Fig. 5E-H) barely impact the

539   lysosomal transport parameters as compared to the control. In contrast, α-synR

540   (Fig. 3E-H) and AßO (Fig. 5E-H) induce significant changes of lysosomes transport

541   parameters (Fig. 2-2*B*). Furthermore, the size of lysosomes significantly increased in

542   the presence of AßO (Fig. 5I-J). This set of impairments of lysosomal transport in

543   Alzheimer-related context are in full agreement with previous reports (Gowrishankar

544   et al., 2015; Marshall et al., 2020). Indeed, using a mouse model of Alzheimer's

545   disease, (Gowrishankar et al., 2015) evidenced axonal lysosome accumulations with

546   local impairment in the retrograde axonal transport of lysosome precursors. Similarly,

547   (Marshall et al., 2020) found that misfolded $Aß_{42}$ impacts the endo-lysosomal

548   pathway. They reported impairments in the uptake of proteins that use a dynamin-

549   dependent endosomal mechanism and accumulation of lysosomes.

Intraneuronal transport of neurodegenerative-related molecular species

550

551   We were able to quantity the intraneuronal transport parameters for α-syn and Aß

552   pathogenic species (Figs 6-7). We found that cargoes loaded with α-synF and R

553   exhibit a more dynamical transport compared to those containing FND that are

554   characterized by a larger pausing frequency and shorter run-length and pausing time

555   (Fig. 6*D*-*G*). AßF and AßO-containing endosomes exhibit similar characteristics

556   (Fig. 7*D*-*G*) with in addition an increase in velocity, not observed for α-synF and R.

557   These results suggest that similar molecular mechanisms are at play in the transport

558   of the two α-syn fibrillar polymorphs, the AßF and AßO. However, the ≈7-fold larger

559   fraction of AßF and AßO found in moving lysosomes compared to α-syn assemblies

560   (Fig. 8), also indicate differences in the molecular interactions of Aß assemblies with

561 lysosomes. These results suggest either a cellular triage leading to differential

562 transport of α-syn and Aß assemblies.

Potential application in drug discovery assay

564 We report here the use of a model based on primary mouse cortical neurons where it

565 is possible to identify a robust decrease in the number of vesicles moving

566 intracellularly (Figs. 2*B*, 3*B*, 4*B* and 5*B*), in the order of 30-50%, and up to 5-fold for

567 lysosomes in neurons exposed to AßO (Fig. 5*B*). Such a large decrease is likely to

568 impact the physiology of neurons and it is reasonable to consider that the transport of

569 other cargoes, such as mitochondria and RNA granules, is also affected. This

570 endolysosomal transport impairment endophenotype can be instrumental in

571 generating large-scale drug-discovery campaigns (*i.e.*, >10^5 compounds) as used in

572 more complex human cellular models (Park et al., 2021).

573 The cargoes transport blockade within cortical neurons we report could either result

574 from a direct interaction between pathogenic aggregates and the intraneuronal

575 transport machinery or a pathogenic aggregates-mediated transcriptional changes in

576 transport proteins expression (Encalada and Goldstein, 2014, Lee et al., 2014; Guo

577 et al., 2020). Analysis of neuronal immuno-precipitates of α-syn fibrillar assemblies

578 and Aß polymorphs may be instrumental to identify the molecular partners that

579 directly interact with these protein assemblies. A recent postmortem proteomics study

580 identified proteins whose abundance changed at different stages of Alzheimer's

581 disease (Li et al., 2021). At its early stage, differentially expressed proteins of

582 "clathrin-coated endocytic vesicle membrane" (GO: 0030669) and the secretory

583 pathway (R-HSA-432720: "Lysosome Vesicle Biogenesis" and R-HSA-432722: "Golgi

584 Associated Vesicle Biogenesis") classes were over-represented. Comparison of

585 proteome profile changes in our neuronal model with (Li et al., 2021) profiles can be

586 instrumental to identify druggable targets in order to enhance the number of
587 transported cargoes.

588 Finally, we quantified intraneuronal transport of neurodegenerative-linked molecular
589 species (α-syn fibrillar polymorphs, AβF and oligomers) whose transport
590 characteristics are distinct from those of endosomes but for which no molecular
591 characterization is yet available. Furthermore, we observed that all these protein
592 assemblies are transported intracellularly in cortical neurons with very similar
593 quantitative characteristics. We could not detect differences in their transport
594 parameters. Further work will be required to identify a possible common transport
595 mechanism and the identification of specific molecules involved in this transport can
596 allow to selectively inhibit it.

597 These results also need to be considered from the standpoint of the prion-like spread
598 of pathogenic protein particles between neurons (Brundin et al., 2010; Hardy and
599 Revesz, 2012; Jucker and Walker, 2018). Selective inhibition may avoid the spread
600 of these neurotoxic species. Thus, advances in the identification of targets involved in
601 cargoes loaded with pathogenic protein aggregates transport may lead to novel
602 neuroprotective therapeutic avenues.

603 ## References

604 Alam P, Bousset L, Melki R, Otzen DE (2019) α-synuclein oligomers and fibrils: a
605 spectrum of species, a spectrum of toxicities. J Neurochem 150(5):522-534.

606 Brahic M, Bousset L, Bieri G, Melki R, Gitler AD (2016) Axonal transport and
607 secretion of fibrillar forms of α-synuclein, $A\beta_{42}$ peptide and HTTExon 1. Acta
608 Neuropathol 131(4):539-48.

609   Braak H, Braak E (1991) Neuropathological stageing of Alzheimer-related changes.

610   Acta Neuropathol 82:239-259.

611   Braak H, Del Tredici K, Ruˑb U, de Vos RAI, Jansen Steur ENH, Braak E (2003)

612   Staging of brain pathology related to sporadic Parkinson's disease. Neurobiol Aging

613   24:197-21.

614   Brundin P, Melki R, Kopito R (2010) Prion-like transmission of protein aggregates in

615   neurodegenerative diseases. Nat Rev Mol Cell Biol 11(4):301-7.

616   Cioni JM, Lin JQ, Holtermann AV, Koppers M, Jakobs MAH, Azizi A, Turner-Bridger

617   B, Shigeoka T, Franze K, Harris WA, Holt CE (2019) Late Endosomes Act as mRNA

618   Translation Platforms and Sustain Mitochondria in Axons. Cell 176(1-2):56-72.e15.

619   Crocker JC, Grier DG (1996) Methods of Digital Video Microscopy for Colloidal

620   Studies. J Colloid Interf Sci 179:298–310.

621   Encalada SE, Goldstein LS (2014) Biophysical challenges to axonal transport: motor-

622   cargo deficiencies and neurodegeneration. Annu Rev Biophys 43:141-69

623   Fernandopulle MS, Lippincott-Schwartz J, Ward ME (2021) RNA transport and local

624   translation in neurodevelopmental and neurodegenerative disease. Nat Neurosci

625   24(5):622-632.

626   Ghee M, Melki R, Michot N, Mallet J (2005) PA700, the regulatory complex of the

627   26S proteasome, interferes with alpha-synuclein assembly. FEBS J272:4023–4033.

628   Giandomenico SL, Alvarez-Castelao B, Schuman EM (2021) Proteostatic regulation

629   in neuronal compartments. Trends Neurosci 3:S0166-2236(21)00161-2.

630   Golde TE, Borchelt DR, Giasson BI & Lewis J (2013) Thinking laterally about

631   neurodegenerative proteinopathies. J. Clin. Invest 123:1847–1855.

25

632 Gowrishankar S, Yuan P, Wu Y, Schrag M, Paradise S, Grutzendler J, De Camilli P,

633 Ferguson SM (2015) Massive accumulation of luminal protease-deficient axonal

634 lysosomes at Alzheimer's disease amyloid plaques. Proc Natl Acad Sci U S A

635 14;112(28):E3699-708.

636 Guo W, Stoklund Dittlau K, Van Den Bosch L (2020) Axonal transport defects and

637 neurodegeneration: Molecular mechanisms and therapeutic implications. Semin Cell

638 Dev Biol 99:133-150.

639 Hardy J, Revesz T (2012) The spread of neurodegenerative disease. N Engl J Med

640 366(22):2126-8.

641 Haziza S, Mohan N, Loe-Mie Y, Lepagnol-Bestel AM, Massou S, Adam MP, Le XL,

642 Viard J, Plancon C, Daudin R, Koebel P, Dorard E, Rose C, Hsieh FJ, Wu CC, Potier

643 B, Herault Y, Sala C, Corvin A, Allinquant B, Chang HC, Treussart F, Simonneau M

644 (2017) Fluorescent nanodiamond tracking reveals intraneuronal transport

645 abnormalities induced by brain-disease-related genetic risk factors. Nat Nanotechnol

646 12(4):322-328.

647 Jucker M, Walker LC (2018) Propagation and spread of pathogenic protein

648 assemblies in neurodegenerative diseases. Nat Neurosci 21(10):1341-1349.

649 Lee WC, Yoshihara M, Littleton JT (2004) Cytoplasmic aggregates trap

650 polyglutamine-containing proteins and block axonal transport in a Drosophila model

651 of Huntington's disease. Proc Natl Acad Sci U S A 101(9):3224-9.

652 Li X, Tsolis KC, Koper MJ, Ronisz A, Ospitalieri S, von Arnim CAF, Vandenberghe R,

653 Tousseyn T, Scheuerle A, Economou A, Carpentier S, Otto M, Thal DR (2021)

654 Sequence of proteome profiles in preclinical and symptomatic Alzheimer's disease.

655 Alzheimers Dement.

656 Liao YC, Fernandopulle MS, Wang G, Choi H, Hao L, Drerup CM, Patel R, Qamar S,
657 Nixon-Abell J, Shen Y, Meadows W, Vendruscolo M, Knowles TPJ, Nelson M,
658 Czekalska MA, Musteikyte G, Gachechiladze MA, Stephens CA, Pasolli HA, Forrest
659 LR, St George-Hyslop P, Lippincott-Schwartz J, Ward ME (2019) RNA Granules
660 Hitchhike on Lysosomes for Long-Distance Transport, Using Annexin A11 as a
661 Molecular Tether. Cell 19;179(1):147-164.e20.

662 Marshall KE, Vadukul DM, Staras K, Serpell LC (2020) Misfolded amyloid-beta-42
663 impairs the endosomal-lysosomal pathway. Cell Mol Life Sci 77(23):5031-5043.

664 De Matteis MA, Luini A (2011) Mendelian disorders of membrane trafficking. N Engl J
665 Med 8;365(10):927-38.

666 Millecamps S, Julien JP (2013) Axonal transport deficits and neurodegenerative
667 diseases. Nat Rev Neurosci 14(3):161-76.

668 Morfini GA, Burns M, Binder LI, Kanaan NM, LaPointe N, Bosco DA, Brown RH,
669 Brown H, Tiwari A, Hayward L, Edgar J, Nave K-A, Garberrn J, Atagi Y, Song Y,
670 Pigino G, Brady ST (2009) Axonal Transport Defects in Neurodegenerative Diseases.
671 J Neurosci 29:12776–12786.

672 Park J-C, Jang S-Y, Lee D, Lee J, Kang U, Chang H, Kim HJ, Han S-H, Seo J, Choi
673 M, Lee DY, Byun MS, Yi D, Cho K-H, Mook-Jung I (2021) A logical network-based
674 drug-screening platform for Alzheimer's disease representing pathological features of
675 human brain organoids. Nat Commun 12:280.

676 Peelaerts W, Bousset L, Van der Perren A, Moskalyuk A, Pulizzi R, Giugliano M, Van
677 den Haute C, Melki R, Baekelandt V (2015) α-Synuclein strains cause distinct
678 synucleinopathies after local and systemic administration. Nature 522(7556):340-4.

679 Renner M, Lacor PN, Velasco PT, Xu J, Contractor A, Klein WL, and Triller A (2010)

680 Deleterious effects of amyloid b oligomers acting as an extracellular scaffold for

681 mGluR5. Neuron 66:739–754.Saez-Atienzar S, Masliah E. Cellular senescence and

682 Alzheimer disease: the egg and the chicken scenario. Nat Rev Neurosci 21(8):433-

683 444.

684 Sardana R, Emr SD (2021) Membrane Protein Quality Control Mechanisms in the

685 Endo-Lysosome System. Trends Cell Biol 31:269–283.

686 Saudou F, Humbert S (2016) The Biology of Huntingtin. Neuron 89(5):910-926.

687 Schindelin J, Arganda-Carreras I, Frise E, Kaynig V, Longair M, Pietzsch T, Preibisch

688 S, Rueden C, Saalfeld S, Schmid B, Tinevez J-Y, White DJ, Hartenstein V, Eliceiri K,

689 Tomancak P, Cardona A (2012) Fiji: an open-source platform for biological-image

690 analysis. Nat Methods 9:676–682.

691 Shrivastava AN, Aperia A, Melki R, Triller A. (2017) Physico-Pathologic Mechanisms

692 Involved in Neurodegeneration: Misfolded Protein-Plasma Membrane Interactions.

693 Neuron 95(1):33-50.

694 Shrivastava AN, Bousset L, Renner M, Redeker V, Savistchenko J, Triller A, Melki R.

695 (2020) Differential Membrane Binding and Seeding of Distinct α-Synuclein Fibrillar

696 Polymorphs. Biophys J 118(6):1301-1320.

697 Shrivastava AN, Kowalewski J.M., Renner M., Bousset L, Koulakoff A, Melki R,

698 Giaume C, and Triller A (2013) ß-amyloid and ATP-induced diffusional trapping of

699 astrocyte and neuronal metabotropic glutamate type-5 receptors. Glia 61:1673–1686.

700 Shrivastava AN, Redeker V, Fritz N, Pieri L, Almeida LG, Spolidoro M, Liebmann T,

701 Bousset L, Renner M, Léna C, Aperia A, Melki R, Triller A. (2015) alpha-synuclein

assemblies sequester neuronal alpha3-Na+/K+-ATPase and impair Na+ gradient. EMBO J 34(19):2408-23.

Shrivastava AN, Redeker V, Pieri L, Bousset L, Renner M, Madiona K, Mailhes-Hamon C, Coens A, Buée L, Hantraye P, Triller A, Melki R. (2019) Clustering of Tau fibrils impairs the synaptic composition of α3-Na+/K+-ATPase and AMPA receptors. EMBO J 38(3):e99871.

Soto C, Pritzkow S (2018) Protein misfolding, aggregation, and conformational strains in neurodegenerative diseases. Nat. Neurosci 21:1332–1340.

Stokin GB, Lillo C, Falzone TL, Brusch RG, Rockenstein E, Mount SL, Raman R, Davies P, Masliah E, Williams DS, Goldstein, LS. (2005) Axonopathy and transport deficits early in the pathogenesis of Alzheimer's disease. Science 307:1282–1288.

Trackpy (2019), doi: 10.5281/zenodo.3492186

Valm AM, Cohen S, Legant WR, Melunis J, Hershberg U, Wait E, Cohen AR, Davidson MW, Betzig E, Lippincott-Schwartz J. (2017) Applying systems-level spectral imaging and analysis to reveal the organelle interactome. Nature 546(7656):162-167.

Victoria GS, Zurzolo C. (2017) The spread of prion-like proteins by lysosomes and tunneling nanotubes: Implications for neurodegenerative diseases. J Cell Biol 216(9):2633-2644.

Volpicelli-Daley LA, Gamble KL, Schultheiss CE, Riddle DM, West AB, Lee VM. (2014) Parkinson's disease Formation of α-synuclein Lewy neurite-like aggregates in axons impedes the transport of distinct endosomes. Mol Biol Cell 25(25):4010-23.

724   Walker LC, Jucker M. (2015) Neurodegenerative diseases: expanding the prion

725   concept. Annu Rev Neurosci 38:87-103.

726   Walsh DM, Thulin E, Minogue AM, Gustavsson N, Pang E, Teplow DB, Linse S

727   (2009) A facile method for expression and purification of the Alzheimer's disease-

728   associated amyloid beta-peptide. FEBS J 276:1266–1281.

729   Winckler B, Faundez V, Maday S, Cai Q, Almeida CG, Zhang H (2018) The

730   Endolysosomal System and Proteostasis: From Development to Degeneration. J

731   Neurosci 38:9364–9374.

732

Figure Legends

Figure 1. Recording fluorescent nanodiamond trajectories in mouse cortical neurons at DIC21. **A**, Schematic representation of the cargoes that are tracked thanks to FND, at different stages after their endocytosis. We previously showed (Haziza et al., 2017) that FND are present in cargos at different stage of their lifetime after endocytosis, as shown by colocalization measurements with specific membrane protein markers: Rab5 for early endosome; Rab7 for late endosome; Rab11 for recycling endosome; Lysotracker for the lysosome. **B**, Illustration of FND trajectories with go (green) and stop (red) phases. **C**, Differential interference contrast images of cortical neurons overlapped with 10 representative trajectories. Scale bar: 10 μm.

Figure 2. Effect of α-synF or R on the mobility of endosomes and their transport as measured by tracking FND-containing cargoes in mouse cortical neurons at DIC21. 24 h exposure to α-synF or R at 0.2 µM concentration, compared to nothing added control (Ctrl). **A,** Number of FNDs detected per field-of-view of 40 µm x 80 µm size during 2 mins of observation. **B**, Fraction of FNDs-containing cargoes having a directed motion. **C**, Length of FND trajectories. **D**, Examples of FND trajectories. Scale bar: 10 μm. **E-H**, Comparison of four transport parameters: **E**, curvilinear velocity, **F**, run length, **G**, pausing time and **H**, pausing frequency. The number within each bar represents the total number of FoV (**A**, **B**) or trajectories (**C**, **E**-**H**) analyzed from *n*=8 coverslips (four independent cultures). Inset: box-plots representation of the same dataset. See also Figure 2-1 and Fig. 2-2.

Figure 3. Effect of α-synF or α-synR on the mobility of LysoTracker-labelled lysosomes and their transport in mouse cortical neurons at DIC21. 24 h exposure to

758　α-synF or α-synR at 0.2 μM concentration, compared to nothing added control (Ctrl).

759　**A**, Number of lysosomes detected per field-of-view of 40 x 80 μm size during 2 mins

760　of observation. **B**, Fraction of lysosomes having a directed motion. **C**, Length of

761　lysosome trajectories. **D**, Examples of lysosome trajectories. Scale bar: 10 μm. **E-H,**

762　Comparison of four transport parameters: curvilinear velocity (**E**), run length (**F**),

763　pausing time (**G**) and **H**, pausing frequency (**H**). The number within each bar

764　represents the total number of FoV (**A**, **B**) or trajectories (**C**, **E**-**H**) analyzed from *n*=2

765　coverslips (from one culture). Inset: box-plots representation of the same dataset.

766

767　**Figure 4.** Effect of AßF and AßO on the mobility of endosomes and their transport as

768　measured by tracking FND-containing cargoes in mouse cortical neurons at DIC21.

769　24 h exposure to AßF and AßO at 1 μM concentration, compared to nothing added

770　control (Ctrl). **A**, Number of FNDs detected per field-of-view of 40 x 80 μm size during

771　2 mins of observation. **B**, Fraction of FNDs-containing cargoes having a directed

772　motion. **C**, Length of FND trajectories. **D**, Examples of FND trajectories. Scale bar:

773　10 μm. **E-H**, Comparison of four transport parameters: curvilinear velocity (**E**), run

774　length (**F**), pausing time (**G**) and pausing frequency (**H**). The number inside the bar

775　represents the total number of FoV (**A**, **B**) or trajectories (**C**, **E**-**H**) analyzed from *n*=6

776　coverslips (three independent cultures). Inset: box-plots representation of the same

777　dataset. See also Figure 4-1.

778

779　**Figure 5**. Effect of AßF and AßO on the mobility of LysoTracker-labelled lysosomes

780　and their transport in mouse cortical neurons at DIC21. 24 h exposure to AßF and

781　AßO at 1 μM concentration, compared to nothing added control. **A**, Number of

782　lysosomes detected per field-of-view of 40 x 80 μm size during 2 mins of observation.

783 **B**, Fraction of lysosomes having a directed motion. **C**, Length of lysosome

784 trajectories. **D**, Examples of lysosome trajectories. Scale bar: 10 μm. **E-H**,

785 Comparison of four transport parameters: curvilinear velocity (**E**), run length (**F**),

786 pausing time (**G**) and pausing frequency (**H**). I-J) Comparison of Lysosome size. The

787 number inside the bar represents the total number of FoV (**A**, **B**), trajectories (**E-H**)

788 and lysosomes (**I**, **J**) analyzed from n=2 coverslips (from one culture). Inset: box-plots

789 representation of the same dataset.See also Figure 5-1, 5-2 and 5-3.

790

791 **Figure 6.** Intraneuronal transport of ATTO 488-labeled α-synF and R in mouse

792 cortical neurons at DIC21. DIC20 cortical neurons were exposed to α-synF and R

793 during 24 h, at concentration of 0.2 μM. **A**-**B**, Examples of α-synF and R, and FND

794 trajectories (in the presence of α-synF and R). Scale bar: 10 μm**. C**, Length of α-synF,

795 α-synR and FND trajectories. **D**-**G**, Comparison of four transport parameters:

796 curvilinear velocity (**D**), run length (**E**), pausing time (**F**) and pausing frequency (**G**).

797 The number inside the bar represents the total number of trajectories analyzed from

798 n=8 coverslips (four independent cultures) is indicated in each bar. Inset: box-plots

799 representation of the same dataset.

800 **Figure 7.** Intraneuronal transport of ATTO 488-labeled AßF and AßO in mouse

801 cortical neurons at DIC21. DIC20 cortical neurons were exposed to AßF and AßO

802 (1 μM) during 24 h. **A**-**B**, Examples of trajectories. Scale bar: 10 μm. **C**, Length of

803 AßF, AßO and FND trajectories. **D**-**G**, Comparison of four transport parameters:

804 curvilinear velocity (**D**), run length (**E**), pausing time (**F**) and pausing frequency (**G**).

805 The number inside the bar represents the total number of trajectories analyzed from
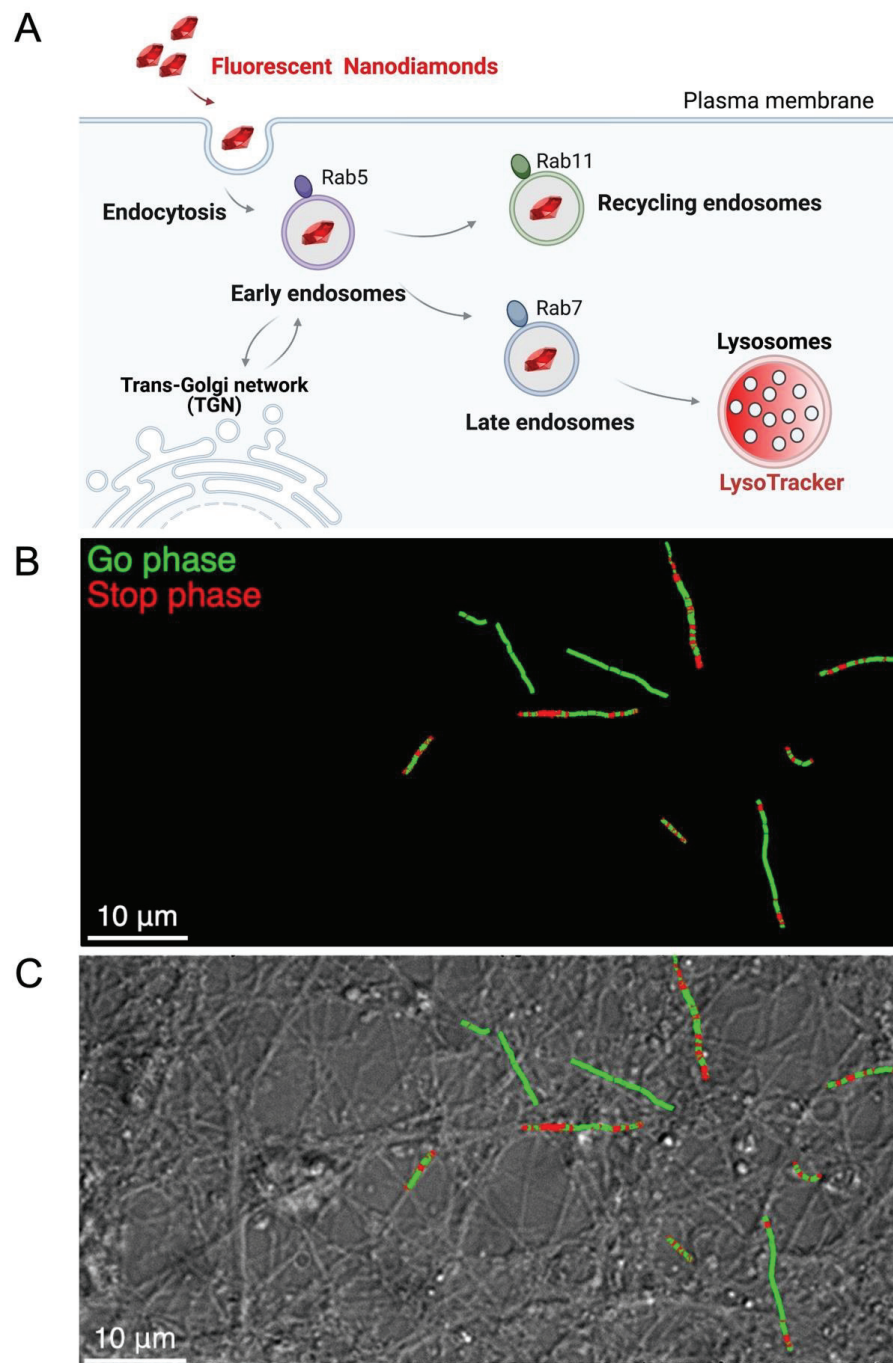
806   *n*=6 coverslips (from three independent cultures) is indicated in each bar. Insets: box

807   plots representation of the same dataset. See also Figure 7-1.

808   **Figure 8.** Colocalized events between moving neurodegenerative disease-related

809   molecular species and moving lysosomes at different time points. *A*, α-synF and α-

810   synR were incubated for 24 and 48 h, at concentration of 0.2 μM. *B*, AßF and AßO

811   were incubated for 24 and 48 h, at concentration of 1 μM. The number inside the

812   donut plot represents the percentage of moving α-syn or Aß assemblies colocalized

813   with lysosomes (LysoTracker labelled). The table on the right panel indicates the

814   number of neurodegenerative-related molecular species trajectories colocalized with

815   lysosomes. n represents the total number of trajectories. The percentage and number

816   of trajectories in each time point were analyzed from 2 coverslips (from one culture).
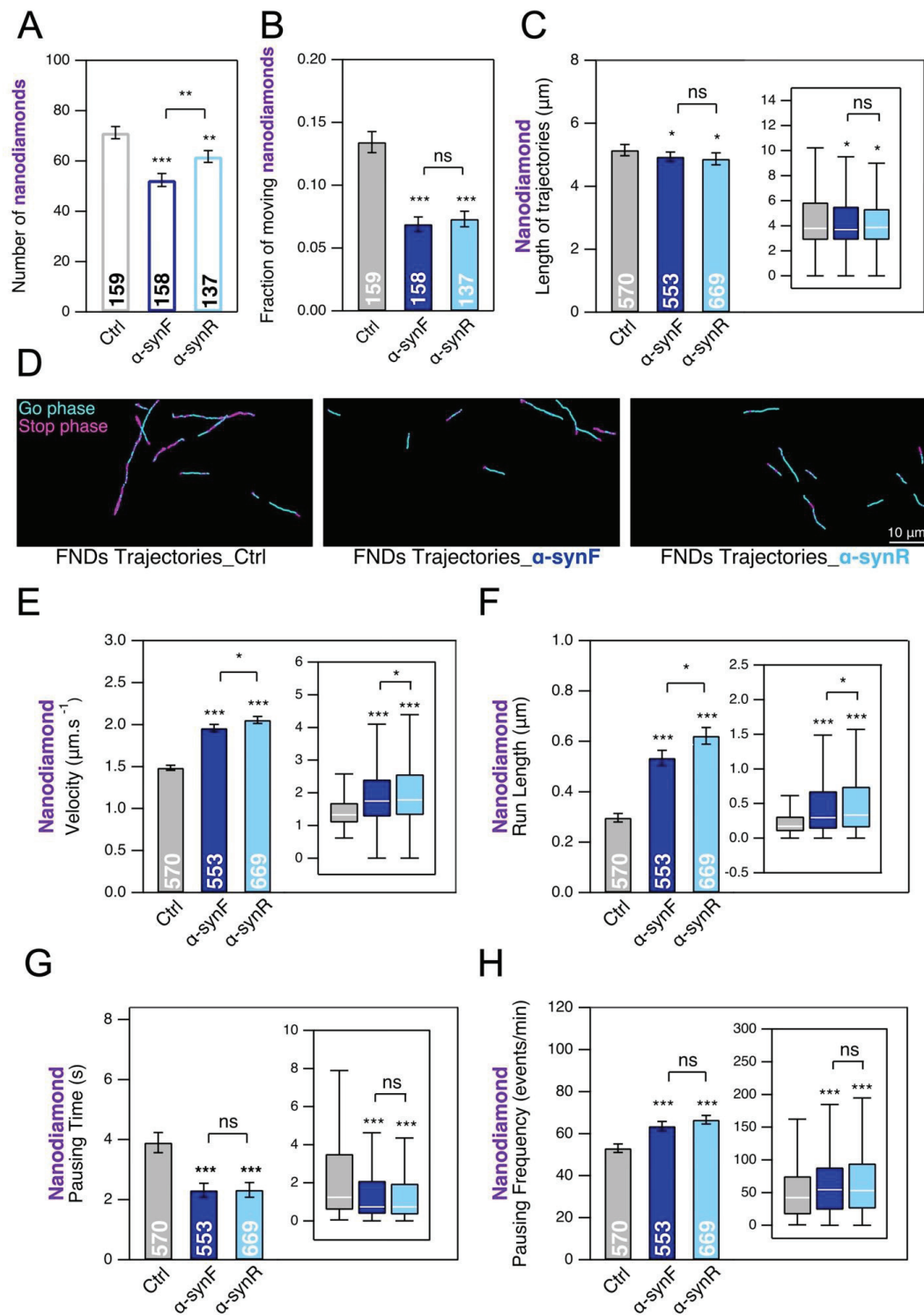
817   See also Figure 8-1.

818
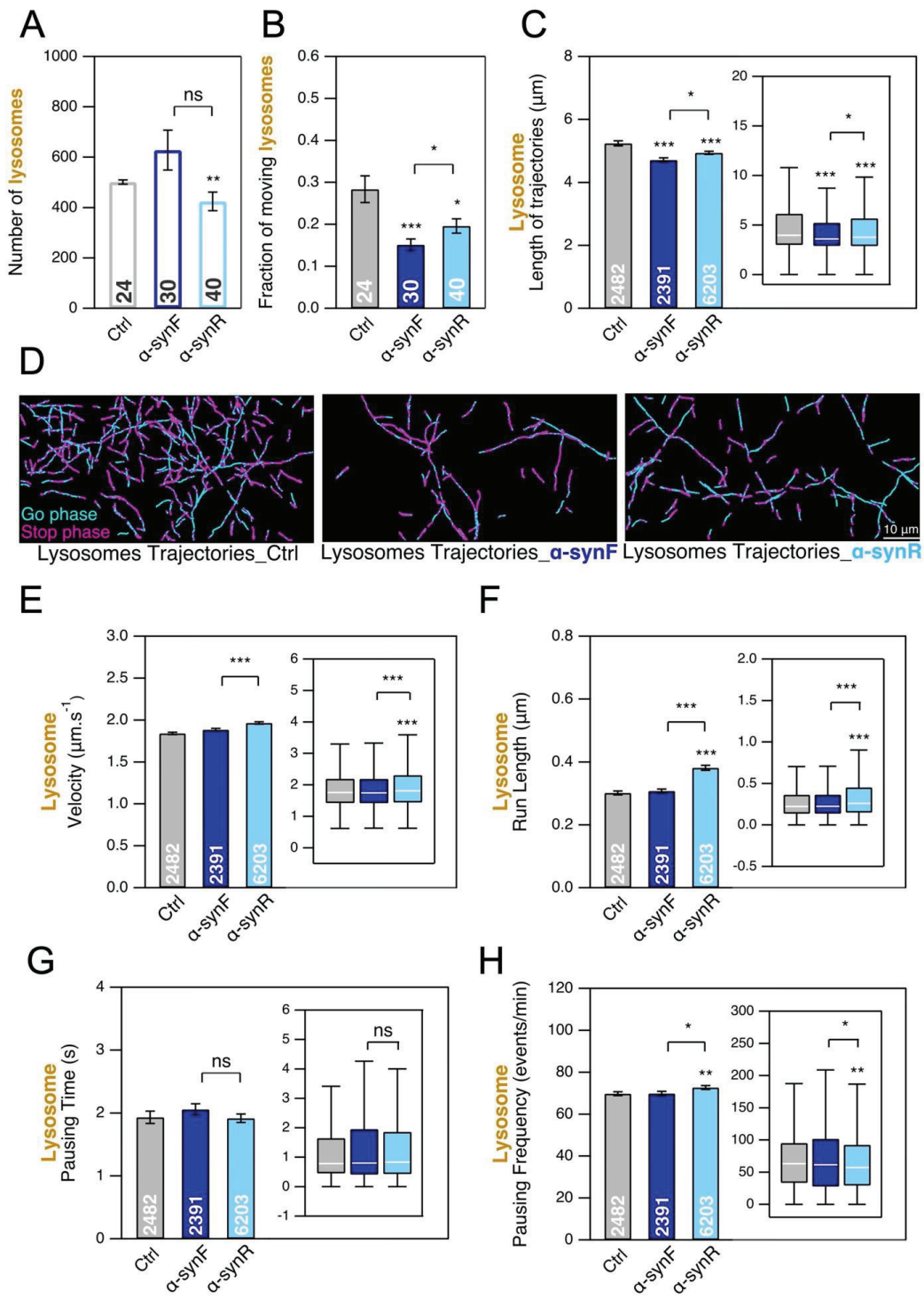
819 **Figures**

820 **Figure 1**

821

822

823   **Figure 2**
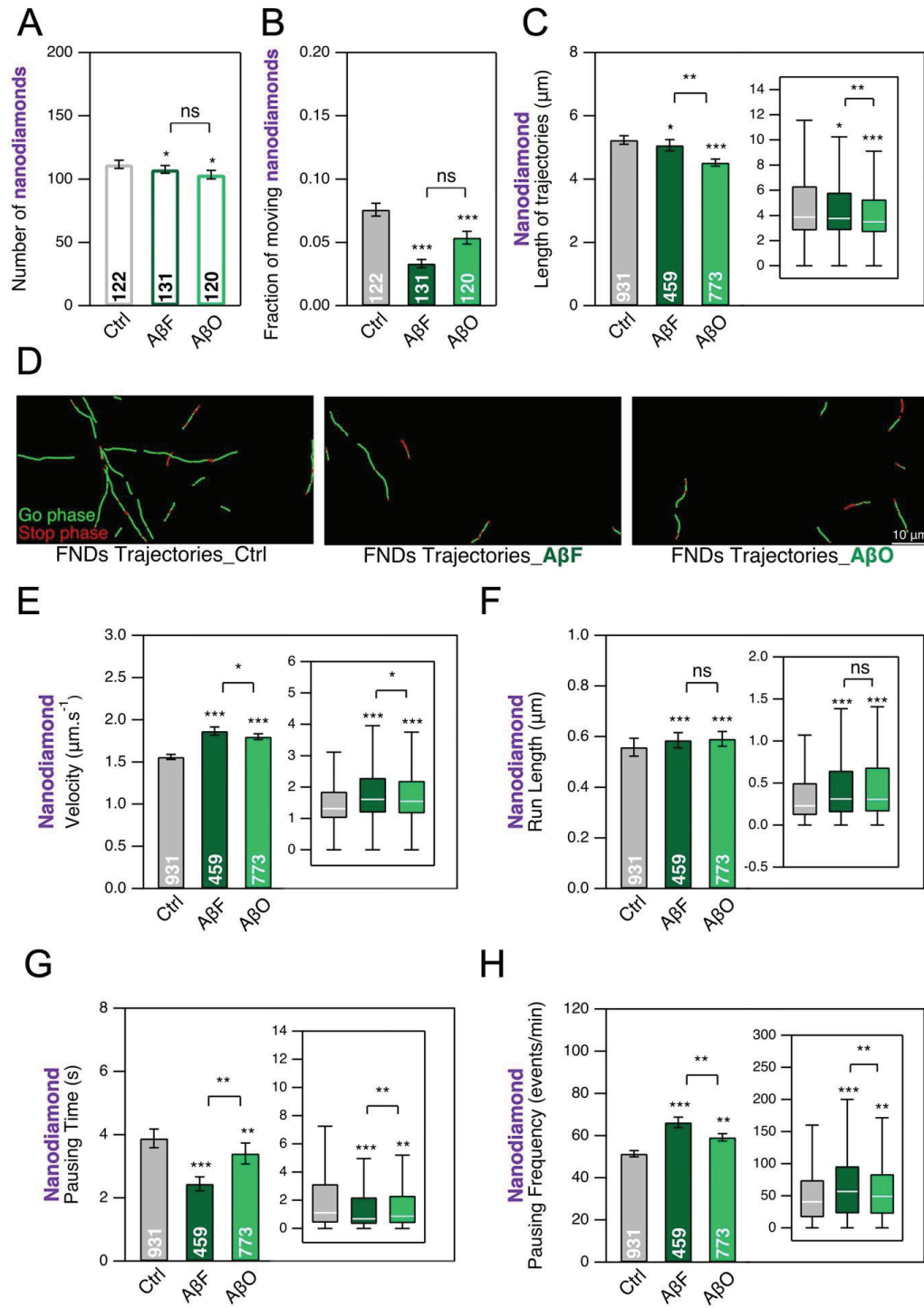
A — Number of nanodiamonds; Ctrl, α-synF, α-synR (159, 158, 137)

B — Fraction of moving nanodiamonds; Ctrl, α-synF, α-synR (159, 158, 137)

C — Nanodiamond Length of trajectories (µm); Ctrl, α-synF, α-synR (570, 553, 669)

D — Go phase / Stop phase
FNDs Trajectories_Ctrl   FNDs Trajectories_α-synF   FNDs Trajectories_α-synR
10 µm

E — Nanodiamond Velocity (µm.s⁻¹); Ctrl, α-synF, α-synR (570, 553, 669)

F — Nanodiamond Run Length (µm); Ctrl, α-synF, α-synR (570, 553, 669)

G — Nanodiamond Pausing Time (s); Ctrl, α-synF, α-synR (570, 553, 669)

H — Nanodiamond Pausing Frequency (events/min); Ctrl, α-synF, α-synR (570, 553, 669)
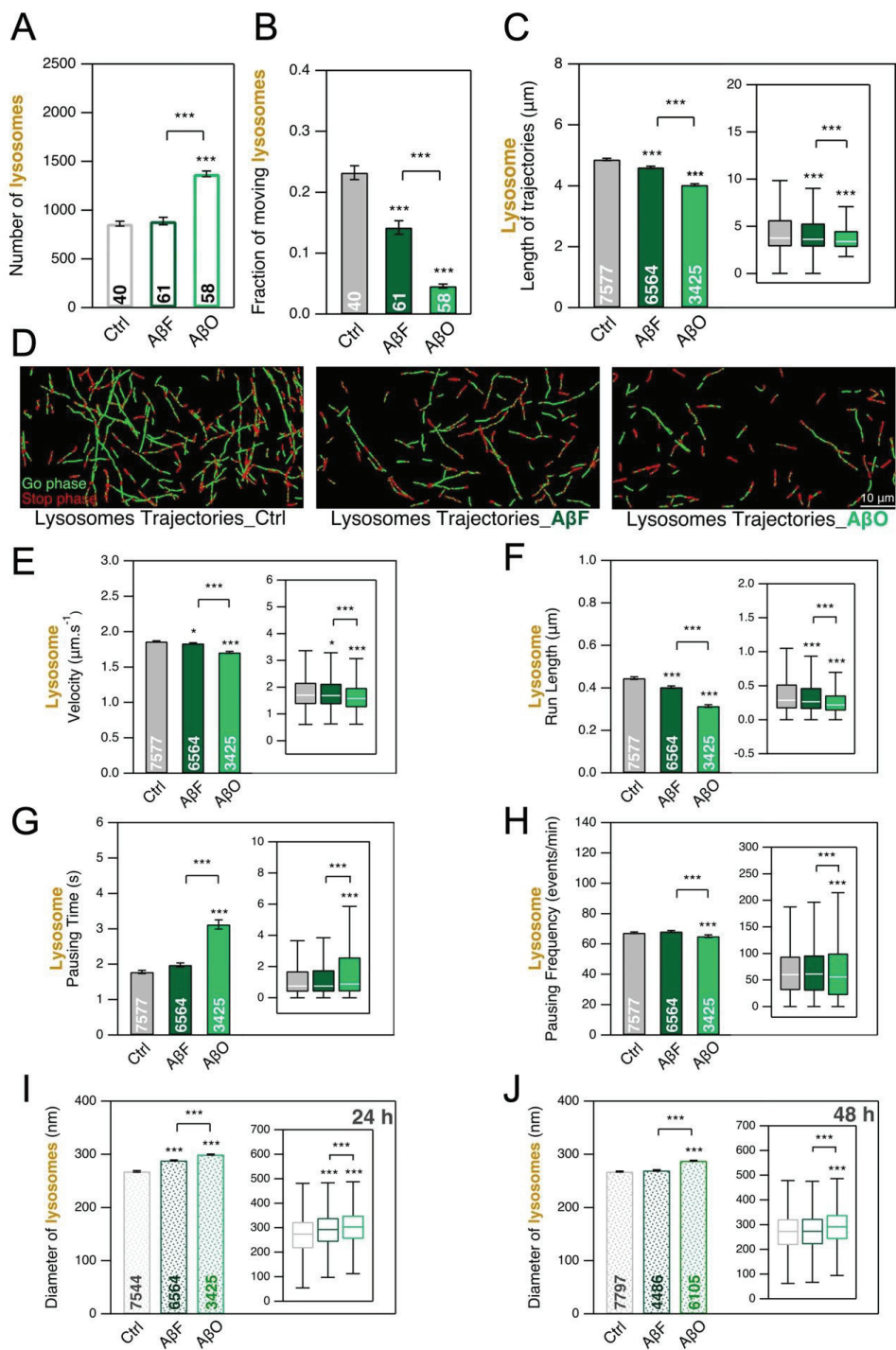
824
825

826 **Figure 3**

827

828

829 **Figure 4**

830

831

832 **Figure 5**
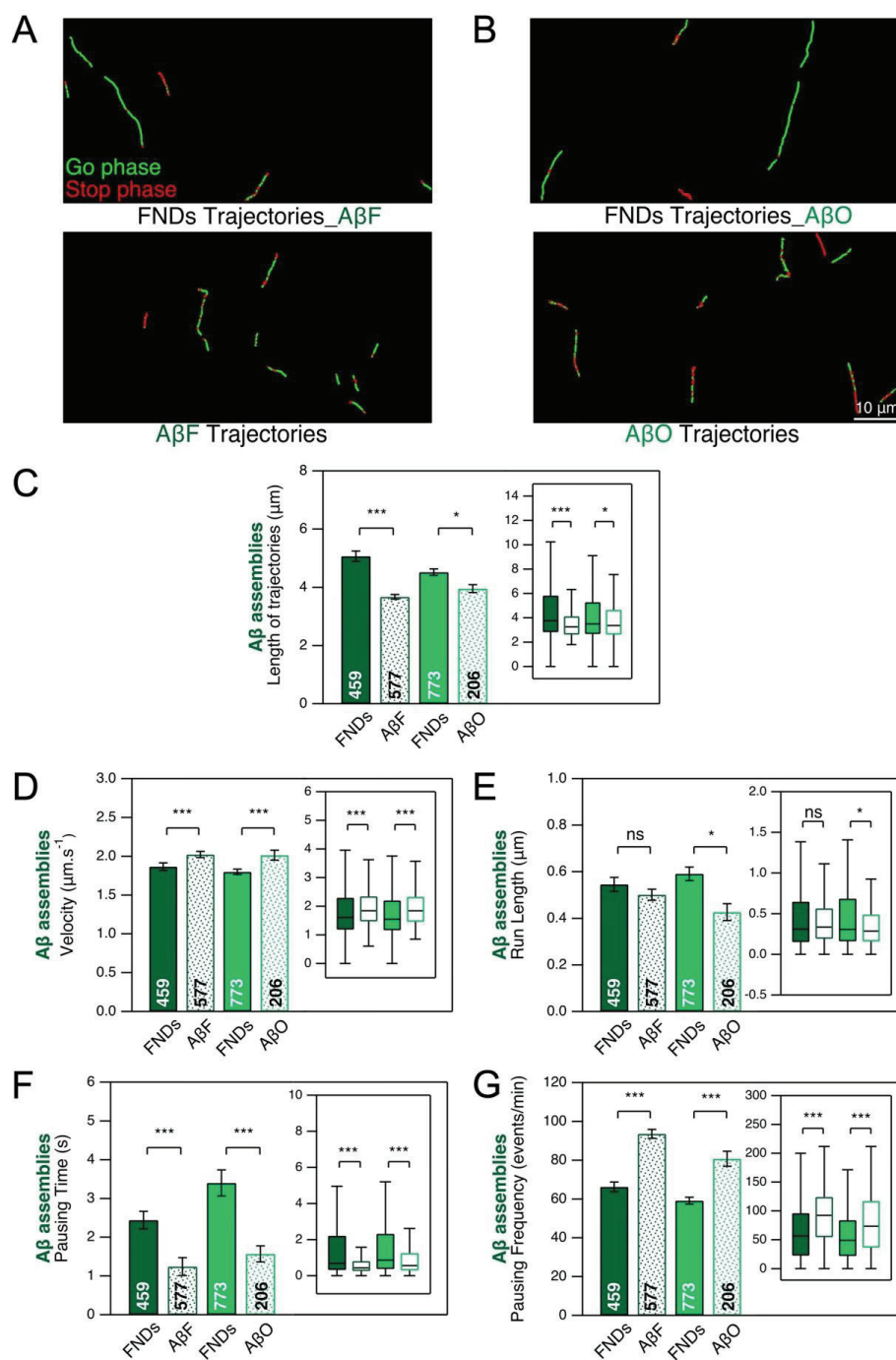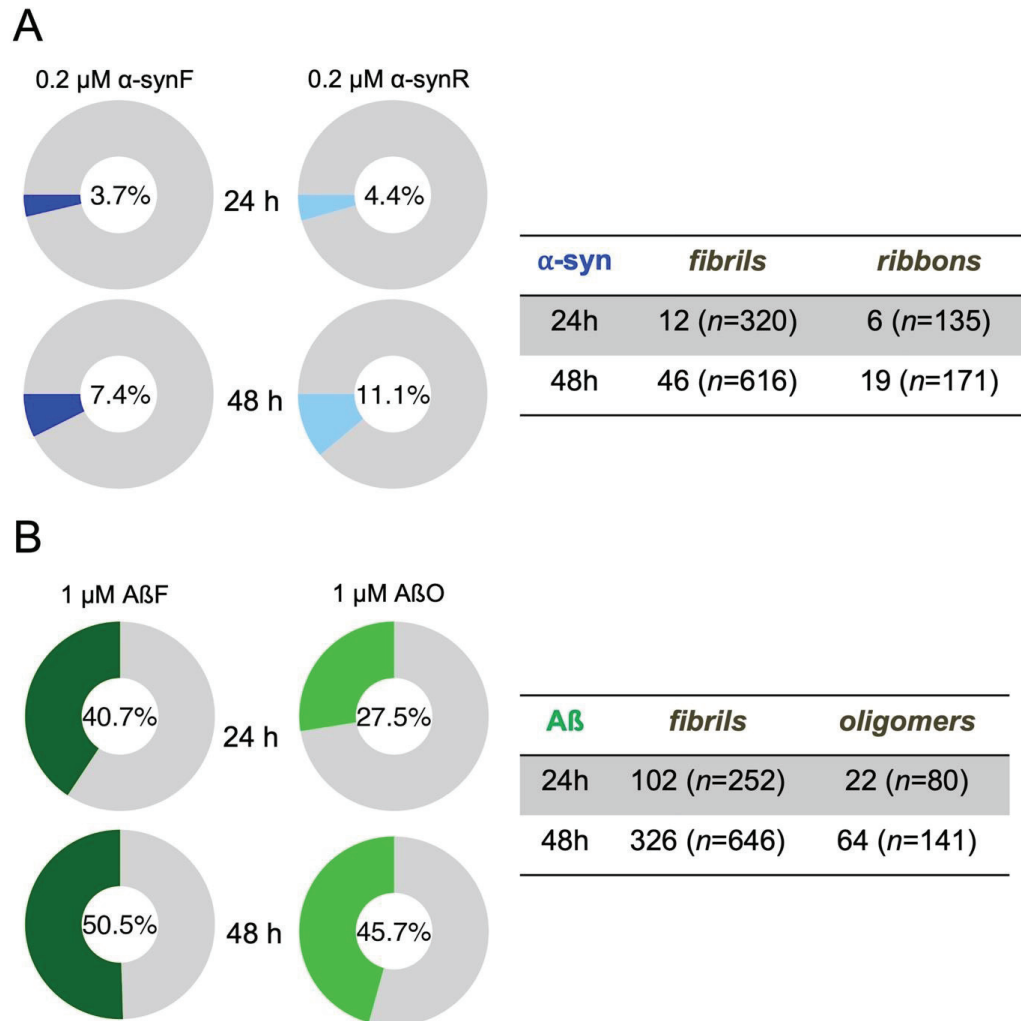

833

834

40

835 **Figure 6**
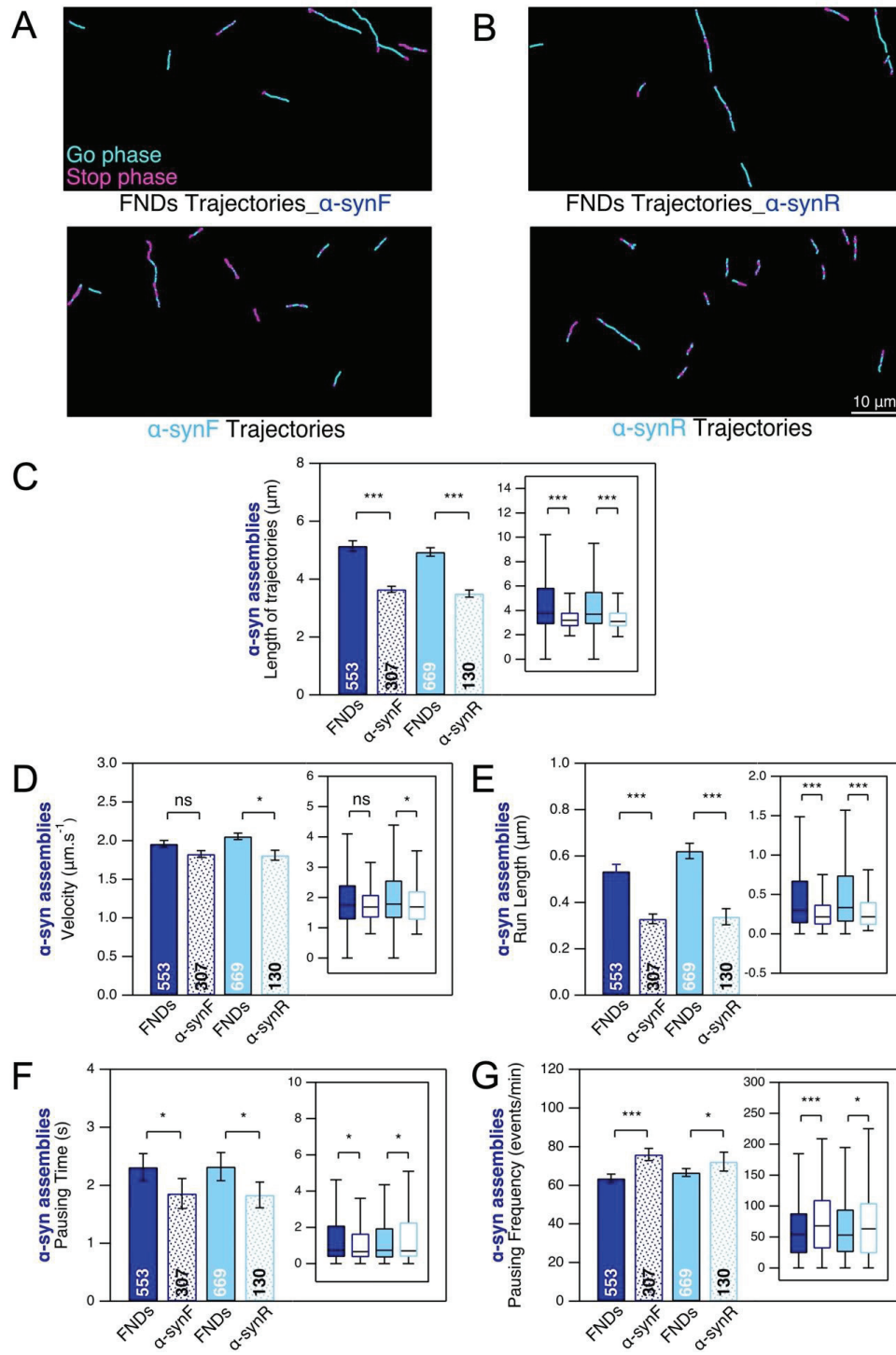
836

837

838 **Figure 7**

839

840

841 **Figure 8**

A

0.2 μM α-synF   0.2 μM α-synR

3.7%   24 h   4.4%

7.4%   48h   11.1%

α-syn	fibrils	ribbons
24h	12 (n=320)	6 (n=135)
48h	46 (n=616)	19 (n=171)

B

1 μM AßF   1 μM AßO

40.7%   24 h   27.5%

50.5%   48 h   45.7%

Aß	fibrils	oligomers
24h	102 (n=252)	22 (n=80)
48h	326 (n=646)	64 (n=141)

842

843

844 **Extended Figure Legends**

845

846 **Figure 2-1.** FNDs interaction with neurons and fluorescence intensity of ATTO 488-

847 labeled α-synF with and without (w/o) washing. 24 h exposure of neurons to α-synF

848 at concentration of 0.2 µM, compared to nothing added control. **A,** Number of FNDs

849 detected per field-of-view of 40 µm x 80 µm during 2 mins of observation for the

850 different conditions. Ctrl: no addition of α-synF; α-synF Wash: addition of α-synF

851 during 24 h and washing of the culture just before addition of FND tracers. Inset: box-

852 plots representation of the same dataset. **B**, Fraction of FNDs-containing cargoes

853 having a directed motion. The numbers inside the bar in A and B represent the total

854 number of FOV analyzed from *n*=2 coverslips (from one culture). **C**, Example of FND

855 trajectories in the different conditions. Scale bar: 10 µm. **D**, Average fluorescence

856 intensity of ATTO 488-labeled α-synF evaluated for 30 µm-long branches, with or w/o

857 washing (*n*= 25 branches from 25 fields-of-view). **E**, Examples of first frames of TIRF

858 videomicroscopy of ATTO 488-labeled α-synF decoration of DIC21 cortical neurons

859 with (top) or w/o (bottom) washing. Scale bar: 10 µm.

860

861 **Figure 2-2.** Summary of the effect of different protein assemblies on the transport

862 parameters of endosomes (**A**), LysoTracker-labeled lysosomes (**B**), and Magic Red-

863 labeled lysosomes (**C**).

864

865 **Figure 4-1.** Impact of Aβ fibrils and oligomers at the concentration of 0.2 µM on the

866 number of nanodiamonds interacting with cells (**A**), on the fraction of moving

867 nanodiamonds (**B**) and on the FND-labelled endosome transport parameters (**C-F**).

868

869 **Figure 5-1.** Lysotracker-labelled compartments size in control (**A**) and 24 h exposure

870 of Aß fibrils (**B**) and oligomers (**C**) at concentration of 1 µM. Scale bar: 2 µm.

871

872 **Figure 5-2.** Effect of α-synF on the mobility of Magic Red-labelled lysosomes and

873 their transport in mouse cortical neurons at DIC21, after 24 h exposure to α-synF at

874 concentration of 0.2 µM, compared to nothing added control. **A**, Number of

875 lysosomes detected per field-of-view of 40 µm x 80 µm size during 2 mins of

876 observation. **B**, Fraction of lysosomes having a directed motion. **C**, Trajectory length.

877 **D**, Examples of lysosome trajectories. Scale bar: 10 µm. **E-H**, Comparison of four

878　transport parameters: **E)** curvilinear velocity (**E**), run length (**F**), pausing time (**G**) and

879　pausing frequency (**H**). **I**, Diameter of Magic Red-labelled lysosomes. General

880　remarks: the number inside the bar represents the total number of FoV (**A**, **B**),

881　trajectories (**E**-**I**). Inset: box-plots representations of the same datasets (**C**-**I**).

882

883　**Figure 5-3.** Effect of AßF on the mobility of Magic Red-labelled lysosomes and their

884　transport in mouse cortical neurons at DIC21 after 24 h exposure to AßF at

885　concentration of 1 µM, compared to nothing added control. **A**, Number of lysosomes

886　detected per field-of-view of 40 µm x 80 µm size during 2 mins of observation. **B**,

887　Fraction of lysosomes having a directed motion. **C**, Trajectory length. **D**, Examples of

888　lysosome trajectories. Scale bar: 10 µm. (**E**-**H**) Comparison of four transport

889　parameters: curvilinear velocity (**E**), run length (**F**), pausing time (**G**) and pausing

890　frequency (**H**). **I**, Comparison of Magic Red-labelled lysosome size. General remarks:

891　The number inside the bar represents the total number of FoV (**A**, **B**) and trajectories

892　(**E**-**I**) Inset: box-plots representation of the same dataset.

893

894　**Figure 7-1.** Number of AßF and AßO trajectories detected per field-of-view of 40 x 80

895　µm during 2 mins of observation. Cortical neurons were exposure to AßF and AßO

896　(1µM) during 24 h (**A**) and 48 h (**B**). The number inside the bar represents the total

897　number of FOV analyzed from n= 6 coverslips (from three cultures) for 24 h and n=2

898　coverslips (from one culture).

899

900　**Figure 8-1**. Fraction of protein assemblies, α-synF (**A**) or AßF (**B**) trajectories

901　colocalizing with Magic Red puncta trajectories, as inferred from the tables indicating

902　the number of protein assembly trajectories colocalizing with Magic Red puncta and

903　the total number of assembly trajectories in parenthesis. Data from 2 coverslips and

904　one culture in both α-synF and Aß cases.

905